Available online at www.sciencedirect.com
SCIENCE DIRECT
Materials Chemistry and Physics 99 (2006) 109–116
MATERIALS CHEMISTRY AND PHYSICS
www.elsevier.com/locate/matchemphys

Optimization of sintering on the structural, electrical and dielectric properties of SnO_2 coated $CuFe_2O_4$ nanoparticles

R. Kalai Selvan [a,b,*], C.O. Augustin [a], C. Sanjeeviraja [b], V.G. Pol [c], A. Gedanken [c]

[a] *Central Electrochemical Research Institute, Karaikudi-630 006, India*
[b] *Department of Physics, Alagappa University, Karaikudi-630 003, India*
[c] *Department of Chemistry, Bar-Ilan University, Ramat-Gan 59100, Israel*

Received 1 June 2005; received in revised form 30 August 2005; accepted 4 October 2005

Abstract

An ever first attempt to synthesize nanocomposites of SnO_2 coated $CuFe_2O_4$ has been made using urea–nitrate combustion method. Effect of various concentrations of SnO_2 (1, 5, 10 and 20 wt.%) at three different sintering temperatures viz., 800, 1000 and 1100 °C for optimizing the compound formation has been studied individually. The synthesized materials were characterized by XRD, TEM, HRTEM, SAED, SEM, FT-IR, UV–vis, electrical conductivity and impedance spectra measurements. The XRD spectra reveal that 1100 °C-sintered sample is of ultra pure and well-defined crystalline nature irrespective of the concentration of SnO_2. The grain size of the materials has been found to get increased as a function of sintering temperature and the extent of SnO_2 substitution. The TEM and HRTEM figures evidence the nanocrystalline nature of the product. SAED pattern confirms the presence of single phase and polycrystalline of the final product. The band gap values were calculated from UV–vis spectra, which confirm the lowest band gap value for the 5 wt.% SnO_2 added sample. The solid-state impedance and the electrical properties of the materials are in favour of the grain and grain boundary effect and the normal behavior of spinel compounds, respectively.

Keywords: Nanocomposites; Spinels; X-ray diffraction; Electrical conductivity

1. Introduction

Nanomaterials are a privileged class of new materials most sought after in recent times, networking with all domain of hi-tech areas. By definition, size of new materials should be less than 100 nm, which are grouped into two following categories: (i) nanocrystals or clusters (quantum dots (1–10 nm)) and (ii) nanowires and tubes (1–100 nm). The nanomaterials are very attractive because of their shape and size dependent properties, which make them superior in various applications compared to the bulk ones. These materials possess high specific surface area, diffusion properties, high density, enhanced electrical, electronic, magnetic, optical, thermal, catalytic, fluorescent, electrochemical and biological properties. Hence nanomaterials of different origins are considered as smart materials useful for fabrication of various devices in all sensitive areas. The use of these compounds will lead to miniaturization and exploitation of their unique properties. The compounds in the realm of active research based on the end uses are spinels, perovskites, garnets, semiconductors, polymers, organometallics and intermetallics.

Basically, nanoferrites with spinel structure are subjected to exhaustive studies owing to their unusual advantageous properties. The general formula of spinel ferrite is $(M_{1-\delta}Fe_{\delta})[M_{\delta}Fe_{2-\delta}]\ O_4$, where, the parenthesis ( ) and [ ] denotes cations sites of tetrahedral and octahedral, respectively, where δ is the inversion parameter. Here $\delta = 0$, it gives normal spinel, $\delta = 1$, gives inverse spinel. The atomic as well as the molecular interactions among the atoms occupying at different crystallographic sites makes the study of such materials important as well as interesting.

Various studies on pure nanoferrite such as Fe_3O_4 [1], $NiFe_2O_4$ [2], $CoFe_2O_4$ [3], $ZnFe_2O_4$ [4] and $MnFe_2O_4$ [5] have shown the supremacy of nanosize in view of their properties and applications. Owing to its superior properties they are used in diverse applications such as anodes for oxidation of organic compounds [6], humidity [7] and gas sensors [8], corrosion resistant materials [9], dyes [10], anticorrosion pigments [11], electrodes for energy devices [12], isolation and purification of genomic DNAs [13], liquefied petroleum gas sensors [14] and green anodes for metallurgical applications [15].

* Corresponding author.
E-mail address: selvankram@rediffmail.com (R.K. Selvan).

0254-0584/$ – see front matter © 2005 Elsevier B.V. All rights reserved.
doi:10.1016/j.matchemphys.2005.10.006

Recently, a new class of nanocomposites prepared from pure ferrites with the incorporation of different oxide matrix attracts the attention of material science researchers, because of their tailor made properties compared to the individual counter parts. Different ferrite based nanocomposites viz., $CoFe_2O_4/SiO_2$ [16], $NiFe_2O_4/TiO_2$ [17], $NiFe_2O_4/SnO_2$ [18], $ZnFe_2O_4/SiO_2$ [19] and $CdFe_2O_4/SiO_2$ [20] have been reported by various authors. Similarly literature is replete with methods such as combustion [21], citrate-gel [22], co-precipitation [23], sonochemical [24], microwave [25], hydrothermal [26], sol–gel [27], mechanochemical [28] and electrochemical methods [29] for preparing nanocomposites of various ferrites.

The present study aims at the synthesis of nanocomposites with a general formula $CuFe_2O_4/x\ SnO_2$ ($x = 0$, 1, 5, 10 and 20 wt.%) by novel urea–nitrate combustion method and the evaluation of structural, morphological, electrical features of the synthesized composites using TEM, HRTEM, X-ray diffraction, Fourier transform infra-red spectroscopy, UV–vis, scanning electron microscope, A.C. conductivity and impedance spectra. The study provides an explorative idea of deploying such green electrodes for possible electrochemical applications in the place of carbon.

2. Experimental

2.1. Synthesis

The nanocrystalline $CuFe_2O_4$ and $CuFe_2O_4/x$ wt.% SnO_2 ($x = 0$, 1, 5, 10 and 20) nanocomposite powders were prepared by urea–nitrate combustion method. The synthesis procedure and the thermodynamical calculations of parent $CuFe_2O_4$ are reported by the same authors elsewhere [30]. The synthetic procedure of composite ferrite ($CuFe_2O_4/SnO_2$) powder is furnished in the flowchart (Fig. 1). The stoichiometric quantities of starting materials viz., $Cu(NO_3)_2{\cdot}6H_2O$, $Fe(NO_3)_3{\cdot}9H_2O$, $SnCl_4$, HNO_3 and $CO(NH_2)_2$ were dissolved in 100 ml distilled water. The mixed nitrate–urea solution was heated at 110 °C, with continuous stirring. After the evaporation of excess of water, a highly viscous gel, known as precursor has been obtained. Subsequently, the gel was ignited at 300 °C to evolve the undesirable gaseous products, resulting in the formation of desired product in the form of foamy powder. Ultimately, the powder was sintered at different temperatures like 800, 1000 and 1100 °C for 5 h to obtain ultrafine powders of $CuFe_2O_4/SnO_2$ nanocomposites.

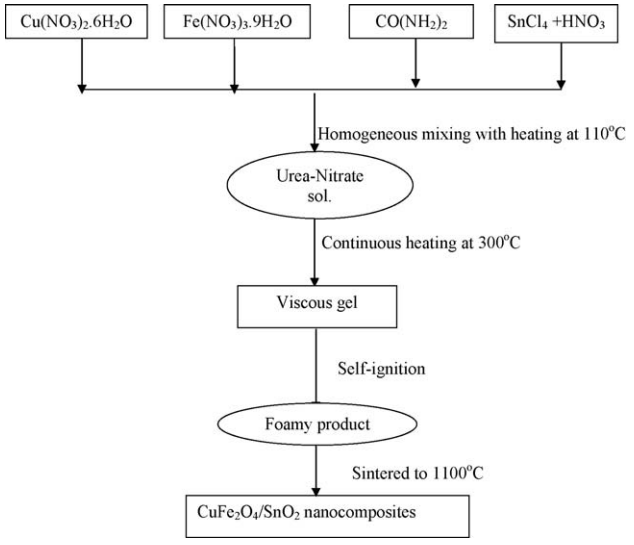

Fig. 1. Flow chart of synthetic method.

2.2. Characterization

The compound formation, phase purity and crystallinity of the ferrite materials were identified by powder X-ray diffraction technique using an X-ray diffractometer (Rigaku Dmax/2C, Japan with Cu Kα radiation; $\alpha = 1.5405$ Å). The nanometric particle size was analyzed through TEM (JEOL-JEM 100SX microscope at an accelerating voltage of 200 kV) respectively. The TEM specimens were prepared by dissolving a small quantity of the sample in ethanol and sonicating the solution for 10 min in a vial placed in a sonication bath. One or two drops of the sample suspension were deposited on a carbon-coated copper grid (400 mesh, Spi suppliers, West Chester, PA, USA) coated with carbon film and allowing them to dry in air, at ambient conditions. The atomic ratios of Cu and Fe were determined by means of EDX analysis using a JEOL-JSM 840 scanning electron microscope. A carbon layer was vacuum vapor-deposited onto the samples to provide a conducting surface. The morphological features have been analyzed through SEM using model JEOL S-3000 Model. The FTIR spectra of samples were recorded using KBr discs in the range of 400–1000 cm^{-1}. Diffuse reflectance spectroscopy measurement was carried out on a Cary Varian 1E spectrometer in the range 200–800 nm. The A.C. impedance measurements are made at room temperature using impedance analyzer HIOKI 3532 controlled by a computer in the frequency range of 42 Hz–5 MHz.

3. Results and discussion

3.1. X-ray diffraction

The diffraction patterns of synthesized nanocrystalline $CuFe_2O_4$ synthesized at various sintering temperatures are shown in Fig. 2. Fig. 2a shows the incomplete formation of poorly crystalline $CuFe_2O_4$, as indicated by the absence of (1 1 1), (4 0 0) etc. peaks and the reduced intensity of (3 1 1) peak, respectively. When the sintering temperature is increased from 300 to 800 °C and 1000 °C, the intensity of $CuFe_2O_4$ peak is increased along with the presence of required newer peaks. In order to enhance the phase purity and crystallinity of the particles has further been sintered at 1100 °C. Interestingly, well-defined sharp peaks with high crystallinity and

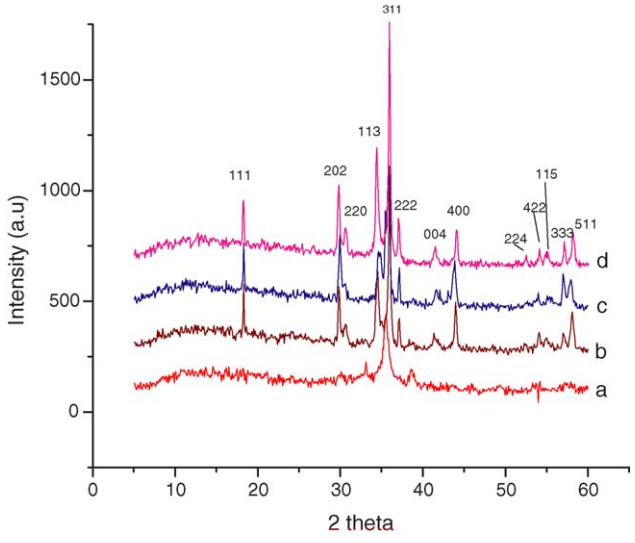

Fig. 2. XRD patterns of $CuFe_2O_4$ of (a) green, (b) sintered at 800 °C, (c) 1000 °C and (d) 1100 °C.

Table 1
XRD parameters

Sample		Green	Sintered at (°C)		
			800	1000	1100
$CuFe_2O_4$	*a* (Å)	8.3737	8.2946	8.2736	8.2740
	c (Å)		8.4256	8.4228	8.4814
	D (nm)	10	13	14	15
$CuFe_2O_4$/1 wt.% SnO_2	*a* (Å)	8.3546	8.2718	8.3510	8.3904
	c (Å)		8.4290	8.4665	8.4189
	D (nm)	15	17	23	25
$CuFe_2O_4$/5 wt.% SnO_2	*a* (Å)	8.3726	8.2939	8.2893	8.4125
	c (Å)		8.4256	8.0515	8.3876
	D (nm)	23	26	28	33
$CuFe_2O_4$/10 wt.% SnO_2	*a* (Å)	8.3986	8.3366	8.2661	8.4082
	c (Å)		8.3964	8.4378	8.3744
	D (nm)	37	41	47	51
$CuFe_2O_4$/20 wt.% SnO_2	*a* (Å)	8.3657	8.3610	8.2708	8.3965
	c (Å)		8.0968	8.5556	8.3860
	D (nm)	39	45	53	58

a,*c*, lattice constants; *D*, grain size.

perfect matching with the standard (PDF no. 6-545) have been obtained for the 1100 °C-calcined product. The presence of peaks corresponding to the planes of (1 1 1), (2 0 2), (2 2 0), (1 1 3), (3 1 1), (2 2 2), (0 0 4), (4 0 0), (0 2 4), (4 2 2), (1 1 5), (3 3 3), (5 1 1) confirm the well defined spinel structure without any impurity, thus indicates that 1100 °C sintering is the optimum sintering temperature to obtain single phase tetragonal $CuFe_2O_4$ formation [31]. The lattice parameter values are given in Table 1 which shows that the as synthesized sample may assume a cubic structure, which will be transformed into a tetragonal phase due to the effect of higher sintering and the Jahn–Teller nature of Cu^{2+} ion. Despite the phase pure formation of $CuFe_2O_4$ at 1000 °C [30] it is further understood from the present study that the 1100 °C-sintered material possesses more cohesive and well-defined peaks of $CuFe_2O_4$. The grain size calculation using Debye–Scherror formula indicates an increase of grain size with increasing temperature due to particle agglomeration.

Fig. 3 shows the XRD patterns for 1100 °C-sintered $CuFe_2O_4$ with the addition of SnO_2 (1, 5, 10 and 20 wt.%). It can be seen that the XRD patterns are well defined with definite '*d*' and '*h k l*' values invariably. The assigned '*h k l*' values infer a marked structural change due to SnO_2 addition. It is further observed that at room temperature both $CuFe_2O_4$ and the SnO_2 added composites are cubic in nature. Moreover no change is observed in the lattice parameter value on SnO_2 addition up to 20%, because of the closer proximity of ionic radii of Cu^{2+} and Sn^{4+}. Unlike the native $CuFe_2O_4$ synthesized at 300 °C (not shown), the SnO_2 added $CuFe_2O_4$ has shown the presence of requisite Bragg peaks even at the lower sintering temperature. This is an indication that SnO_2 addition has aided the process of sintering towards the formation of $CuFe_2O_4$ composites in a better manner. Thus, the added SnO_2 is found to play a role of flux towards the synthesis of nanocrystalline copper ferrite composites and the said effect is clearly evident. For the 1100 °C-sintered samples, the XRD pattern is found to be sharp and highly intense.

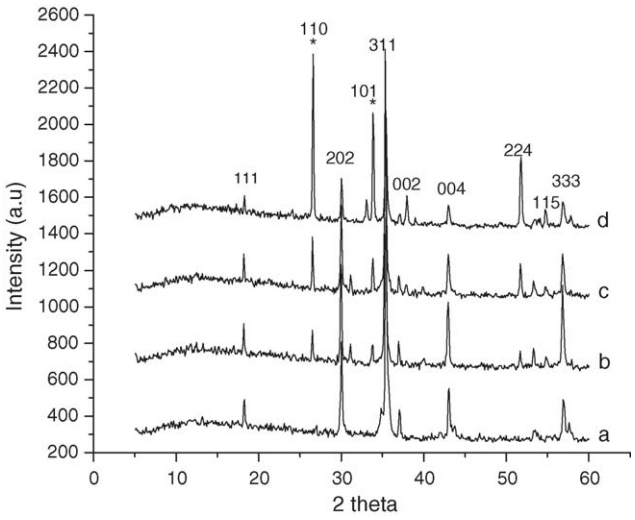

Fig. 3. XRD patterns of 1100 °C-sintered $CuFe_2O_4/x$ SnO_2 composites. (a) $x = 1$, (b) $x = 5$, (c) $x = 10$ and (d) $x = 20$. (*) SnO_2.

Concerning the SnO_2 addition, 5% SnO_2 added composites exhibit prominent (3 1 1) peak of $CuFe_2O_4$ compared to 10 and 20% samples. Further, intensities of (1 1 0) and (1 0 1) peaks assigned for SnO_2 are found to increase with the increasingly added SnO_2. An interesting observation made for the 20% SnO_2 composition is the suppression of the (3 1 1) prominent $CuFe_2O_4$ peak in contrast to (1 1 0) and (1 0 1) peaks. This can be attributed to the solubility limit of SnO_2 in $CuFe_2O_4$ as it can remain well within 20 wt.% only. Hence it is concluded from XRD studies that a sintering temperature of 1100 °C is the optimum temperature to synthesize phase pure and better crystalline SnO_2 coated $CuFe_2O_4$ composites. Therefore the study has further been oriented towards the optical, vibrational, morphological and electrical characteristics of nanocomposites synthesized solely at 1100 °C for better understanding of the potential candidate towards practical applications.

3.2. TEM, HRTEM and SEM analysis

Fig. 4a and b shows the TEM and HRTEM images of nanocrystalline $CuFe_2O_4$ obtained by urea–nitrate combustion method. It is obvious from Fig. 4a that the particles are uniformly dispersed with an average particle size of 10–20 nm. The HRTEM (Fig. 4b) images show the well-defined lattice fringes that may be attributed to nanocrystallinity of the as synthesized product and superiority of the combustion synthesis. The calculated interlayer spacing of 2.51 Å is equal to the "*d*" value of (3 1 1) plane for the tetragonal phase of $CuFe_2O_4$. The selected area electron diffraction (SAED) (Fig. 4c) pattern shows the formation of ring patterns, which also indicates the nanocrystalline nature as well as the best match of XRD '*d*' spacing. The energy dispersive X-ray analysis (EDX) (Fig. 4d) reveals the elemental analysis of $CuFe_2O_4$, which is more or less equal to the molecular weight ratio. Trace amount of carbon residue has

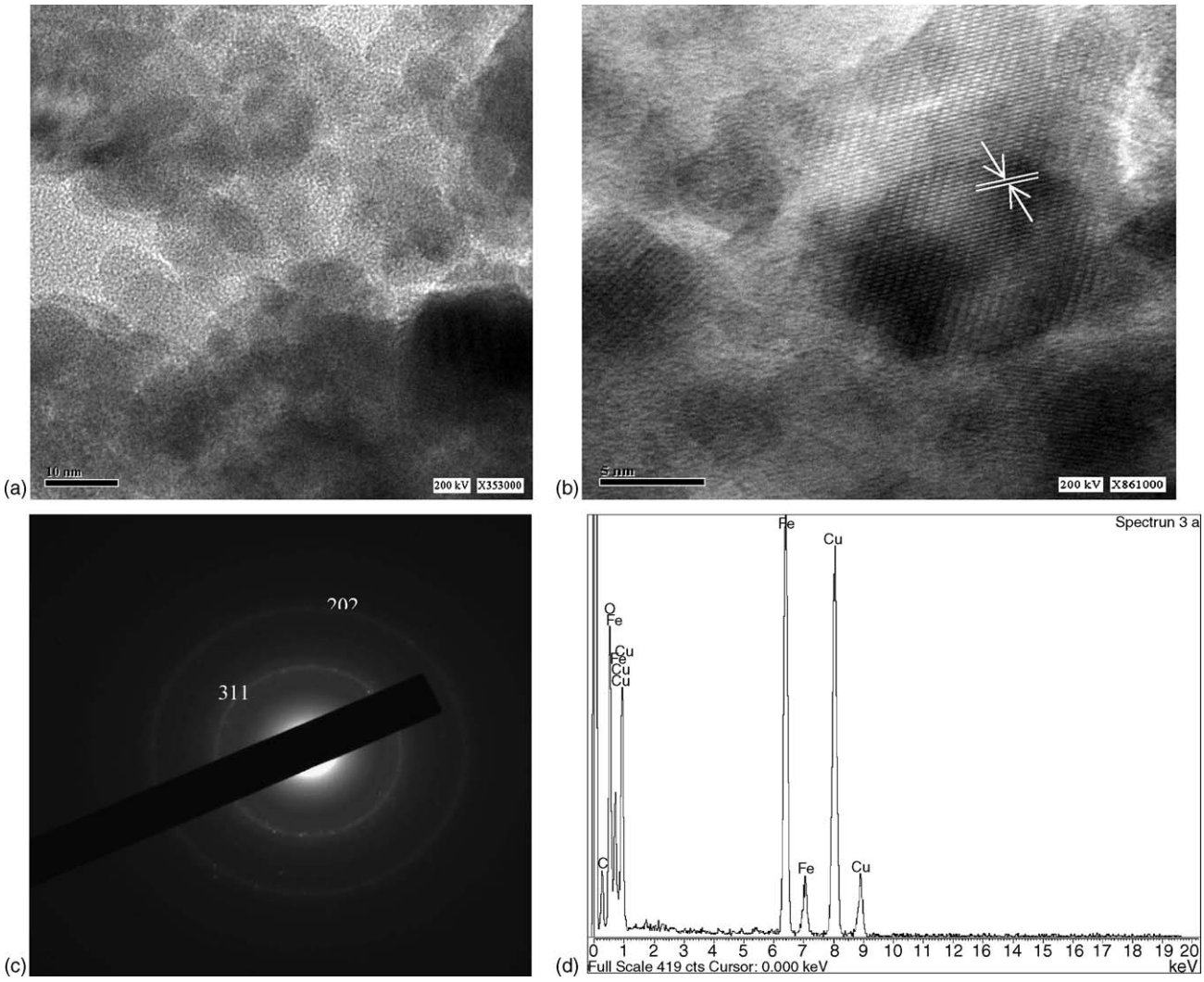

Fig. 4. (a) TEM images of $CuFe_2O_4$, (b) HRTEM images of $CuFe_2O_4$, (c) SAED patterns of $CuFe_2O$ and (d) EDX analysis of $CuFe_2O_4$.

been identified along with the elements, which might have come from the urea.

The TEM and HRTEM images of SnO_2 coated $CuFe_2O_4$ nanocomposite is shown in Fig. 5a and b. The TEM (Fig. 5a) picture visualizes the non-magnetic SnO_2 coated on single crystalline $CuFe_2O_4$ particles. The individual grains are uniformly distributed with an average particle size of 20–30 nm. The HRTEM (Fig. 5b) images show the well-defined lattice fringes, which in turn confirm the crystalline nature of the ferrite seed particles. The SnO_2 layer that has been coated on the ferrite particles are also clearly seen in HRTEM recorded for 5% SnO_2 added $CuFe_2O_4$ nanocomposites. The SAED (Fig. 5c) pattern indicates the spot patterns, which shows the polycrystalline structure of the particles, which is also reflected in XRD.

The SEM images (Fig. 6a and b) show the morphological features of 1100 °C-sintered $CuFe_2O_4/x$ SnO_2 ($x = 0$ and 5 wt.%) nanocomposites. The individual grains are well separated by the grain boundaries and the grain size is much larger compared with TEM results due to the high temperature sintering. One advantage is that the particles are uniformly grown and not agglomerated which may be due to the particle size confinement effect. The 5% SnO_2 added particle gives the smaller grain size than other composites, thereby favours the 5 wt.% SnO_2 addition as the optimum one as indicated by XRD results.

3.3. FTIR and UV–vis spectra

Fig. 7 shows the FTIR spectra of combustion synthesized $CuFe_2O_4/SnO_2$ nanocomposites recorded between 400 and 1400 cm^{-1}. The spectra elucidate the position of cations in the crystal structure with oxygen ions and their vibrational modes, which represents the various ordering positions of the structural properties of the compositions. In ferrite the metal cations are situated in two different sub-lattices namely tetrahedral (A-sites) and octahedral (B-sites) according to the geometric configuration of the oxygen ion nearest neighbors. The band υ_1 around 600 cm^{-1} is attributed to stretching vibration of tetrahedral complexes and υ_2 around 400 cm^{-1} to that of octahedral complexes. Due to the stretching vibration of Fe^{3+}–O^{2-} for tetrahedral sites [30], all the systems show only one-absorption band at 577.36, 578.50, 574.28, 577.65 and 574.46 cm^{-1} for $CuFe_2O_4$, $CuFe_2O_4$/1 wt.% SnO_2, $CuFe_2O_4$/5 wt.% SnO_2,

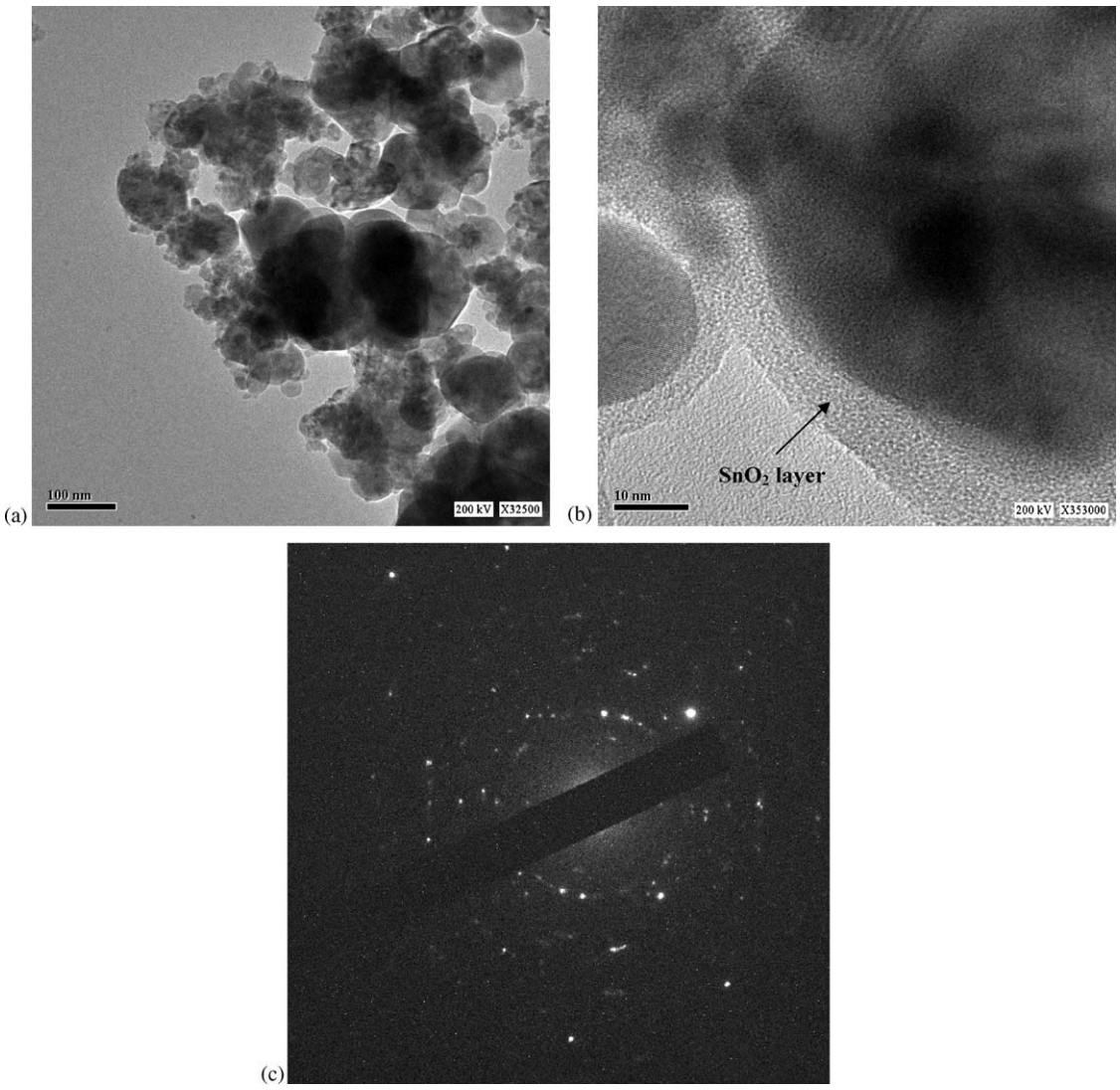

Fig. 5. (a) TEM images of $CuFe_2O_4$/5 wt.% SnO_2 nanocomposites, (b) HRTEM images of $CuFe_2O_4$/5 wt.% SnO_2 nanocomposites and (c) SAED patterns of $CuFe_2O_4$/5 wt.% SnO_2 nanocomposites.

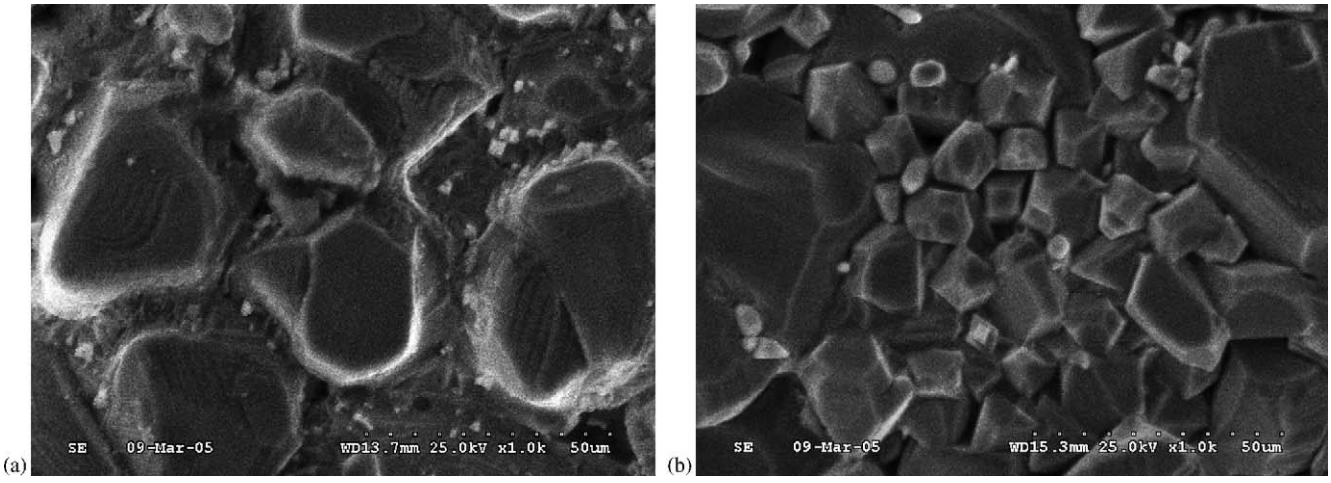

Fig. 6. SEM micrographs of (a) 1100 °C-sintered $CuFe_2O_4$ and (b) $CuFe_2O_4$/5 wt.% SnO_2.

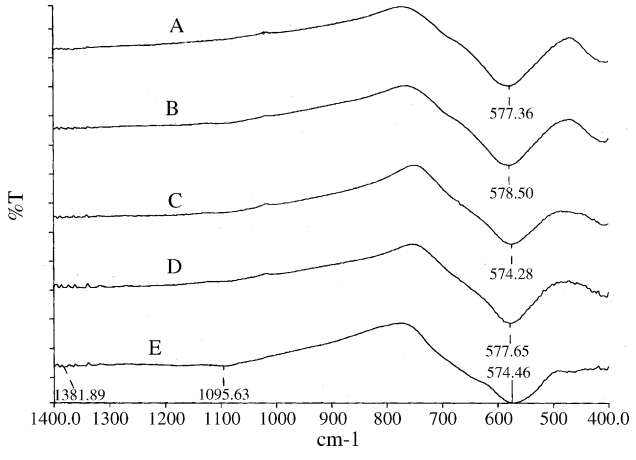

Fig. 7. FT-IR spectra of $CuFe_2O_4/x$ wt.% SnO_2 sintered at 1100 °C, (A) $x = 0$, (B) $x = 1$, (C) $x = 5$, (D) $x = 10$ and (E) $x = 20$.

$CuFe_2O_4$/10 wt.% SnO_2 and $CuFe_2O_4$/20 wt.% SnO_2, respectively. The octahedral complexes may not present within the experimental range, because the band position is nearly 400 cm^{-1}.

The UV–vis spectra of 1100 °C-sintered $CuFe_2O_4/x$ SnO_2 ($x = 0$, 1, 5, 10 and 20 wt.%) nanocomposites are shown in Fig. 8. From the spectra, the optical band gap values are calculated using fundamental absorption edge. The absorption edge was defined as the wavelength at intersection that was obtained by extrapolating the horizontal and sharply rising portion of UV–vis absorption curve [32]. The calculated band gap values are 2.63, 2.55, 2.50, 2.91 and 3.07 eV for the above nanocomposites. The observed band gap values reflect the vicinity of semiconducting nature.

3.4. A.C. electrical conductivity

Fig. 9 shows the A.C. electrical conductivity of $CuFe_2O_4/SnO_2$ ($x = 0$, 1, 5, 10 and 20 wt.%) measured at room temperature from 42 Hz to 5 MHz. It can be seen that

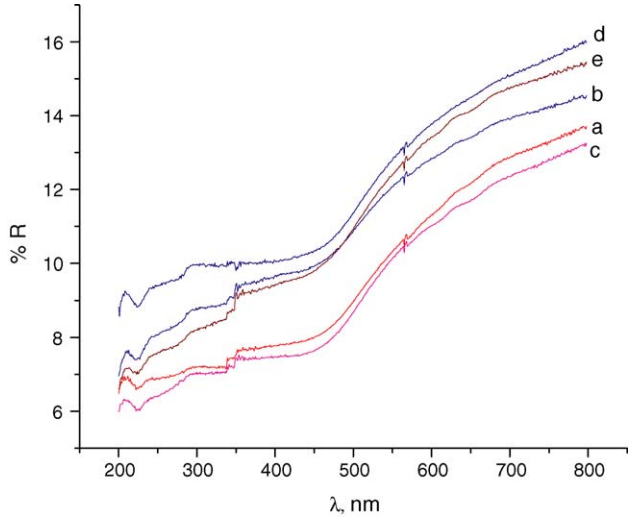

Fig. 8. UV–vis spectra of $CuFe_2O_4/x$ wt.% SnO_2 sintered at 1100 °C, (a) $x = 0$, (b) $x = 1$, (c) $x = 5$, (d) $x = 10$ and (e) $x = 20$.

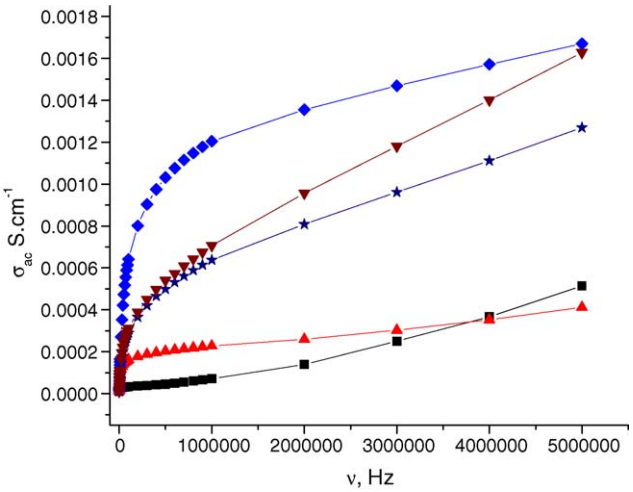

Fig. 9. A.C. conductivity vs. frequency for $CuFe_2O_4/x$ wt.% SnO_2 sintered at 1100 °C, (■) $x = 0$, (▲) $x = 1$, (◆) $x = 5$, (★) $x = 10$ and (▼) $x = 20$.

all the samples show frequency dependent behavior, typical of semiconducting materials. The conduction in ferrite has been explained by using hopping mechanism of charge carriers at B-sites. The applied frequency enhances the hopping frequency as well as the mobility of charge carriers resulting an increase in the conductivity. The rate of increase in conductivity of $CuFe_2O_4$ is observed to be very low when compared with other samples. The following redox reactions may be suggested for the competing conduction mechanism of $CuFe_2O_4$.

$Fe^{2+} \Leftrightarrow Fe^{3+} + e^-$ (for electronic conduction),

$Cu^{2+} \Leftrightarrow Cu^{+} + e^+$ (for hole conduction).

As expected the 5% SnO_2 added sample gives the maximum conductivity of 1.669 S cm^{-1}. The maximum concentration of SnO_2 (≥10 wt.%) gives lower conduction due to larger grain growth. Similarly Sn^{4+} has strong preference to occupy octahedral sites and has a tendency to shift some Fe^{3+} ions from B-sites to A-sites [33]. Hence the active charge carrier concentration of Fe^{3+} for conduction in octahedral site is reduced, decreasing the electronic transitions between Fe^{2+} and Fe^{3+} ions ultimately resulting a decrease in conductivity.

3.5. Dielectric constant

The dielectric property of semiconductor materials mainly depends upon the method of preparation, chemical composition, grain size, calcination temperature and applied frequency. Fig. 10 shows the variation of dielectric constant with frequency for $CuFe_2O_4/x$ SnO_2 ($x = 0$, 1, 5, 10 and 20 wt.%) nanocomposites measured at room temperature from 42 Hz to 5 MHz. It shows a normal dielectric behavior of typical semiconducting materials, which is due to Maxwell interfacial polarization. According to Maxwell–Wagner model, the dielectric structure of spinel ferrite is mainly due to inhomogeneous nature of materials [34] arising from high temperature sintering. The individual high conducting grains are separated by low conducting grain boundaries due to calcinations. The polarization results in an electronic

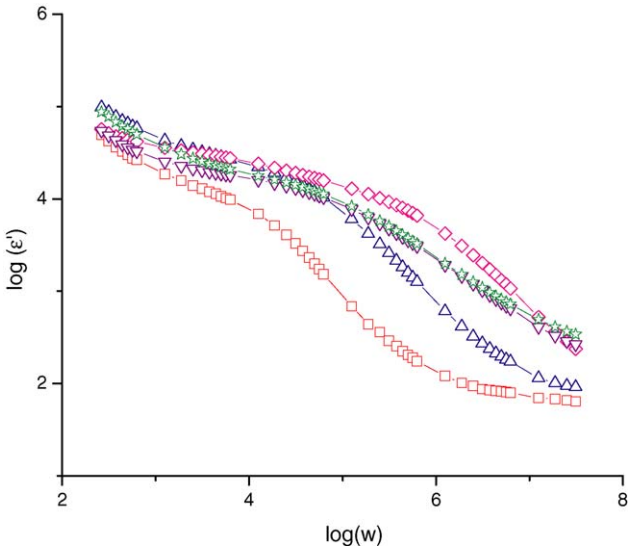

Fig. 10. Dielectric constant vs. frequency for $CuFe_2O_4/x$ wt.% SnO_2 sintered at 1100 °C, (□) $x = 0$, (△) $x = 1$, (◇) $x = 5$, (☆) $x = 10$ and (▽) $x = 20$.

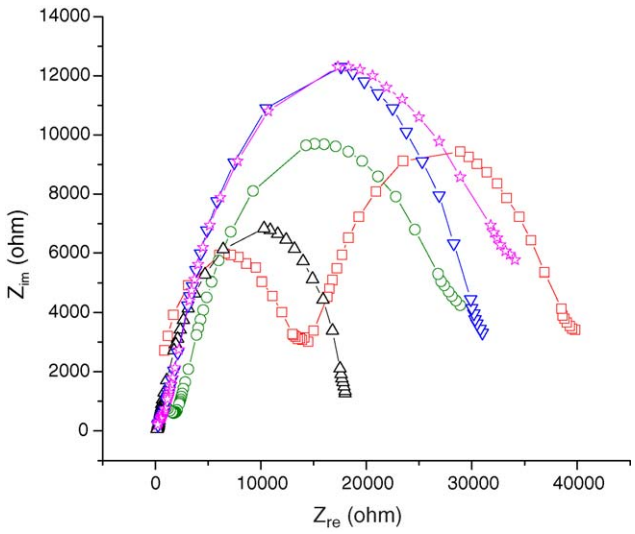

Fig. 11. Solid-state impedance spectra of $CuFe_2O_4/x$ wt.% SnO_2 sintered at 1100 °C, (□) $x = 0$, (○) $x = 1$, (△) $x = 5$, (▽) $x = 10$ and (☆) $x = 20$.

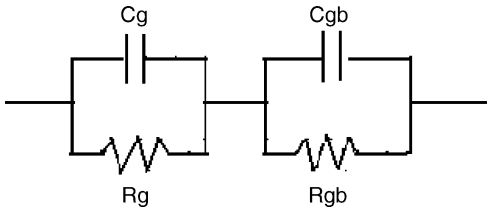

Fig. 12. Equivalent circuit of $CuFe_2O_4$.

exchange between the ferrous and ferric ions, which produce local displacements in the direction of applied external field. Similarly the $Cu^{2+} \Leftrightarrow Cu^{+} + e^{+}$ gives the hole concentration in the octahedral sites, which produce the local displacements in the opposite direction of the applied field. These displacements determine the polarization as well as the dielectric properties. The decrease in dielectric constant with increasing frequency is due to the fact that the electronic exchange between the Fe^{3+} and Fe^{2+} ions cannot follow the external applied frequency. Fig. 10 also explains the compositional dependence of dielectric constant with frequency. The dielectric constant values of composites are high compared with parent ferrite, which may be explained in line with the conducting mechanisms.

3.6. Impedance spectra

The impedance spectrum is an important tool to understand the origin of conducting mechanism such as whether it is due to grain effect or grain boundary effect. Fig. 11 shows that the $CuFe_2O_4$ has two semicircular arcs, due to grain boundary effect and an arc in high frequency side due to grain interior effect. When the concentration of SnO_2 increases, surprisingly it gives only one arc due to grain effect. According to Brick layer model, the equivalent circuit based on the impedance spectra of $CuFe_2O_4$ is shown in Fig. 12, where R_g, R_{gb} and C_g, C_{gb} are the grain and grain boundary resistance and grain and grain boundary capacitance, respectively. When the SnO_2 addition increases, 5% sample gives lower resistance due to higher conductivity. The equivalent circuit of composite materials is the parallel combination of C_g and R_g. This is the intra grain phenomenon [35]. Fig. 13 shows the variation of real part (Z') of impedance with frequency. It can be seen that the impedance values are monotonically decreased with increasing frequency except for $CuFe_2O_4$. High impedance value is observed at low frequency side due to the space charge polarization. The decreasing impedance with increasing frequency enumerates the increasing conductivity of all the samples. At high frequency side the impedance value is merged due to the release of space charge carriers as a result of lowering the barrier properties [36]. Fig. 14 shows the variation of imaginary part of the impedance spectra (Z'') with frequency for various concentration of SnO_2 measured at room temperature. The impedance loss spectra of $CuFe_2O_4$ show two peaks and other samples show only one peak. Compared with $CuFe_2O_4$, the peak height, i.e. the magnitude of impedance is

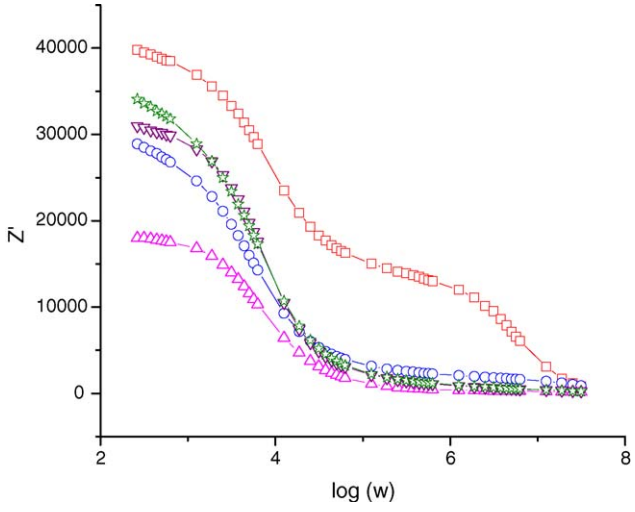

Fig. 13. Real part of impedance spectra of $CuFe_2O_4/x$ wt.% SnO_2 sintered at 1100 °C, (□) $x = 0$, (○) $x = 1$, (△) $x = 5$, (▽) $x = 10$ and (☆) $x = 20$.

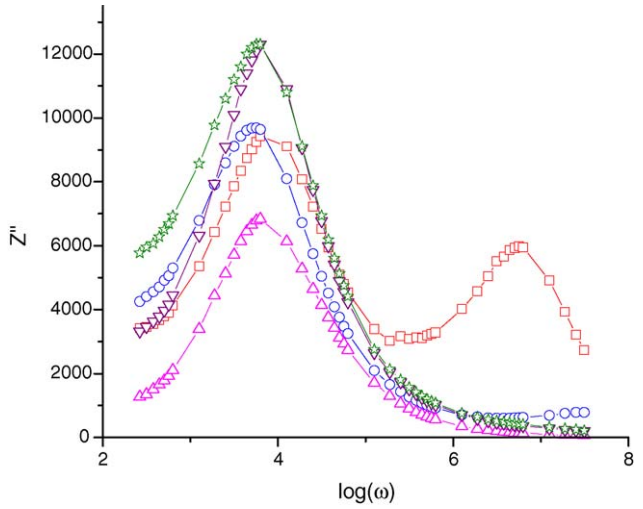

Fig. 14. Imaginary part of impedance spectra of $CuFe_2O_4$/x wt.% SnO_2 sintered at 1100 °C, (□) $x = 0$, (○) $x = 1$, (△) $x = 5$, (▽) $x = 10$ and (☆) $x = 20$.

increased with increasing addition of SnO_2. The spectra of all the SnO_2 added samples merge at high frequency side due to the electrical relaxation phenomena of charge carriers of electrons and excess added SnO_2.

4. Conclusions

In the present investigation, a new class of nanocomposites of $CuFe_2O_4$ with SnO_2 additives has been prepared by adopting urea–nitrate combustion method. The XRD pattern confirms the possibility of synthesizing single-phase copper ferrite with poly crystalline composite at 1100 °C. The TEM studies show that the synthesized copper ferrite and its composites are nanocrystalline with an average particle size of 10–30 nm. The HRTEM images confirmed the coating of SnO_2 layer upon copper ferrite. The presence of well-defined grains with definite size has been confirmed from SEM features. The FTIR spectra revealed characteristic stretching and bending vibrations of ferrites. The semiconductor range of the synthesized materials was confirmed from the optical band gap values derived from UV–vis spectra. The A.C. electrical conductivity and dielectric constant infers frequency dependent behavior and the impedance spectra confirm the grain and grain boundary effect for conduction.

Acknowledgement

The authors express their gratitude to Prof. S. Selvasekarapandian, Department of Physics, Bharadhiar University, Coimbatore for extending the facility of A.C. electrical studies. The authors are very much grateful to Prof. A.K. Shukla, Director, CECRI for his kind interest.

References

[1] R. Abu Mukh-Qasem, A. Gedanken, J. Colloid Interface Sci. 284 (2005) 489.
[2] Huaming Yang, Xiang Chau Zhang, Weigin Ao, Guanzhou Qiu, Mater. Res. Bull. 39 (2004) 833.
[3] Kim E. Mooney, Zennifer A. Nelson, Michael J. Wagner, Chem. Mater. 16 (2004) 3155.
[4] M. Veith, M. Haas, V. Huch, Chem. Mater. 17 (2005) 95.
[5] Christy R. Vestal, Z. John Zhang, J. Am. Chem. Soc. 125 (2003) 9828.
[6] C.G. Raman Kutty, S. Sugunan, Appl. Catal. A 218 (2001) 39.
[7] A.Y. Lipare, P.N. Vasambekar, A.S. Vaingankar, Mater. Chem. Phys. 81 (2003) 108.
[8] Nai-Sheng Chen, Xiao-Juan Yang, Er. Sheng Liu, Jin-Ling Huang, Sens. Actuators B 66 (2000) 178.
[9] Li Yuchun, Zhou Tao, Zhoukechas, Liu Yong, Liu Fang, Zhang Fang, Anti Corr. Methods Mater. 51 (2004) 6.
[10] Jian Hua Meng, Gui Qin Yang, Lemei Yan, Xiu Yu Wang, Dyes Pigments 66 (2005) 109.
[11] A. Kalendora, D. Vesely, J. Brodinova, Anti Corr. Methods Mater. 51 (2004) 6.
[12] Yan-Na Nuli, Yan-Qiu Chu, Qi-Zong Qin, J. Electrochem. Soc. 151 (2004) A1077.
[13] J. Pradelalova, B. Rittich, A. Spanova, K. Petrova, M.J. Benes, J. Chromatogr. A 1056 (2004) 43.
[14] L. Satyanarayana, K. Madhusudan Reddy, Sunkara V. Manorama, Mater. Chem. Phys. 82 (2003) 21.
[15] L. John Berchmans, R. Kalai Selvan, C.O. Augustin, Mater. Lett. 58 (2004) 1928.
[16] R.C. Pedroza, S.W. da Silva, M.A.G. Soler, P.P.C. Sartoratto, D.R. Rezende, P.C. Morais, J. Magn. Magn. Mater. 289 (2005) 139.
[17] Y.S. Chung, S.B. Park, D.W. Kang, Mater. Chem. Phys. 86 (2004) 375.
[18] A.S. Albuquerque, J.D. Ardisson, W.A.A. Macedo, T.S. Plivelic, I.L. Torriani, J. Larrea, J.E.B. Saitovitch, J. Magn. Magn. Mater. 272–276 (2004) 2211.
[19] Z.H. Zhou, J.M. Xue, H.S.O. Chan, J. Wang, Mater. Chem. Phys. 75 (2002) 181.
[20] J. Plocek, A. Hutlova, D. Niznansky, J. Bursik, J.L. Rehspringer, Z. Micka, J. Non-Cryst. Solids 315 (2003) 70.
[21] C.O. Augustin, K. Hema, L. John Berchmans, R. Kalai Selvan, R. Saraswathi, Phys. Stat. Solidi A 202 (2005) 1017.
[22] C.O. Augustin, R. Kalai Selvan, R. Nagaraj, L. John Berchmans, Mater. Chem. Phys. 89 (2005) 406.
[23] Satyabrata Si, A. Kotal, T. Mandal, S. Giri, H. Nakamura, T. Kohara, Chem. Mater. 16 (2004) 3489.
[24] A. Gedanken, Ultrason. Sonochem. 11 (2004) 47.
[25] F. Bensebaa, F. Zavaliche, P.L. Euuyer, R.W. Cochrame, T. Veres, J. Colloid Interface Sci. 277 (2004) 104.
[26] J.F. Wang, C.B. Ponton, R. Grossinger, I.R. Harris, J. Alloys Compd. 369 (2004) 170.
[27] M. Poporici, MartiGich, D. Niznansky, A. Roig, G. Chouteau, J. Nogues, Chem. Mater. 16 (2004) 5542.
[28] F. Padella, C. Alvani, A. La Barbera, G. Ennas, R. Liberatore, F. Varsano, Mater. Chem. Phys. 90 (2005) 172.
[29] S.D. Sartale, G.D. Bagde, C.D. Lokhande, M. Giersig, Appl. Surf. Sci. 182 (2001) 366.
[30] R. Kalai Selvan, C.O. Augustin, L. John Berchmans, R. Saraswathi, Mater. Res. Bull. 38 (2003) 41.
[31] S. Amazen, H.M. Zaki, Phys. Stat. Solidi A 199 (2003) 305.
[32] C. Wang, B. Xu, J. Solid State Chem. 177 (2004) 3448.
[33] S. Balaji, R. Kalai Selvan, L. John Berchmans, S. Angappan, K. Subramanian, C.O. Augustin, Mater. Sci. Eng. B 119 (2005) 119.
[34] A.K. Singh, T.C. Goel, R.G. Mendiratta, O.P. Thakur, C. Prakash, J. Appl. Phys. 91 (2002) 6626.
[35] S. Brahma, R.N.P. Choudhary, A.K. Thakur, Physica B 355 (2005) 188.
[36] S. Sen, R.N.D. Choudhary, Mater. Chem. Phys. 87 (2004) 256.